Double Helix of Atomic Displacements in Ferroelectric $PbTiO_3$

Yihao Hu (胡逸豪)[1,2,*] and Shi Liu (刘仕)[2,3,†]

[1] *Zhejiang University, Hangzhou, Zhejiang 310058, China*

[2] *Department of Physics, School of Science, Westlake University, Hangzhou, Zhejiang 310030, China*

[3] *Institute of Natural Sciences, Westlake Institute for Advanced Study, Hangzhou, Zhejiang 310024, China*

Abstract

Recent theoretical work has predicted the existence of a "dipole spiral" structure in strained freestanding membranes of $PbTiO_3$, suggesting a potential route to enhanced electromechanical responses [PRL **133**, 046802 (2024)]. However, its microscopic nature, energetic landscape, and electronic properties remain largely unexplored from a first-principles perspective. Here, using density function theory on $PbTiO_3$ under biaxial tensile strain, we identify a novel form of polar order: a chiral, non-collinear ferroelectric double helix. We find that two distinct, intertwined polarization helices are formed by the local Pb-O and Ti-O dipoles, reminiscent of DNA. This topology is stabilized by a collective helical twisting of the encompassing oxygen cages (the polyhedra for both Pb and Ti cations), which gives rise to an electric Dzyaloshinskii-Moriya-like interaction. The resulting structure, which can be canceptualized as a "self-moiré" crystal, exhibits two coupled functionalities. First, it possesses a rotational pseudo-zero-energy mode that underpins a giant piezoelectric response ($e_{33} \approx 16$ C/m^2). Second, the long-period potential reconstructs the electronic band structure, leading to a multi-valley electronic topology at the valence band edge. Our work establishes a physical route to designing complex chiral order that supports both giant electromechanical coupling and multi-valley electronics.

Keywords: Ferroelectrics; Piezoelectrics; Density functional theory; Dipole spiral

* huyihao@westlake.edu.cn

† liushi@westlake.edu.cn

The past decade has witnessed a surge of interest in topological polar structures within ferroelectric oxides. Real-space textures such as polar vortices [1–3], skyrmions [4, 5], and merons [6], analogous to their magnetic counterparts, have been realized. These discoveries have demonstrated that by carefully balancing elastic, electrostatic, and polarization-discontinuity gradient energies through epitaxial strain and interfacial engineering [7], one can overcome the strong crystalline anisotropy of ferroelectrics and stabilize complex, non-collinear polarization patterns. Helical structures are ubiquitous in nature, manifesting across all length scales. From the spiral arms of galaxies to the turbulent vortices of weather systems, down to the intricate spin helices that drive multiferroicity in quantum materials [8, 9], this chiral form represents an elegant solution to complex energetic constraints. Perhaps most iconically, the double helix of DNA encodes the fundamental blueprint of life itself. A compelling question thus arises in condensed matter physics: can a similar helical order be realized for electric dipoles within a crystalline solid, and what new physics would such a "ferroelectric helix" unlock?

The realization of helical order arising from competing interactions is a well-established concept in modern magnetism, but achieving an analogous helical texture of electric dipoles has remained challenging. One notable development was the experimental observation of an incommensurate helical dipole texture in the chemically doped quadruple perovskite $BiCu_{0.1}Mn_{6.9}O_{12}$, which was shown to be stabilized by an intrinsic competition between lone-pair activity and orbital ordering [10]. In parallel, theoretical work has proposed a distinct route toward ferroelectric helicity: stabilizing a "dipole spiral" in the archetypal ferroelectric $PbTiO_3$ under large in-plane biaxial tensile strain [11]. Unlike the very small out-of-plane polarization ($< 20\ \mu C/m^2$) in $BiCu_{0.1}Mn_{6.9}O_{12}$, this phase in $PbTiO_3$ exhibits a stable out-of-plane ferroelectric polarization comparable to that of the conventional tetragonal (T) phase ($0.7\ C/m^2$), making it a potential example of a ferroelectric helix. Moreover, this topological structure has been associated with a potentially enhanced piezoelectric response, pointing to a mechanism for electromechanical coupling that may be rooted in the underlying topology. These findings motivate further investigation into the microscopic origin and functional implications of such a phase. Despite recent interest, a comprehensive understanding of this helical phase from a first-principles perspective remains incomplete. Key questions persist regarding its microscopic structure, energetic stability relative to conventional ferroelectric phases, the origin of its functional properties, and the extent to which

it modifies the material's electronic behavior.

Here, we employ density functional theory (DFT) calculations to investigate the fundamental physics of the emergent phase in strained $PbTiO_3$. Our results indicate that the dipole spiral corresponds to a ferroelectric double helix. Specifically, we find that the local Pb-O and Ti-O dipoles form two distinct, intertwined helical paths with a stable, non-parallel phase relationship between them. The stability of this configuration can be traced to a collective helical twisting of the oxygen octahedral framework, which gives rise to an electric Dzyaloshinskii-Moriya-like interaction (eDMI) [12, 13]. This chiral structure, which may be viewed as an one-dimensional "self-moiré" crystal, exhibits a rotational pseudo-zero-energy mode that contributes to its enhanced piezoelectric response. Furthermore, we find that the structural topology leads to a reconstruction of the electronic band structure, resulting in a multi-valley electronic character at the valence band edge. Overall, our work outlines a theoretical framework that links structural chirality, emergent eDMI, electromechanical response, and electronic band topology, offering insights into potential design strategies for multifunctional polar materials.

Our first-principles calculations for $PbTiO_3$ under substantial biaxial tensile strain indicate the stabilization of a ground state that differs from conventional ferroelectric phases (see Supplemental Material (SM) [14], Sec.IV). The system adopts a set of chiral dipole spirals, topological polar structures that bear analogy to spin spirals in magnetic materials [15, 16]. A key geometric feature of this phase is its helical character, which we quantify using the Ti-cation displacement d_{Ti} as a proxy for local polarization [17], though this is only a partial measure chosen for its convenience as a descriptor. Specifically, the dipoles under 2.3% strain ($a = b = 3.970$ Å) in a 1×1×5 supercell, tilted by θ_z from the z axis (Fig. 1a), exhibit in-plane components $d_{\mathrm{Ti},xy}$ with approximately equal magnitudes in each layer, while the azimuthal angle rotates progressively from one layer to the next; the out-of-plane components $d_{\mathrm{Ti},z}$ remain largely unchanged. This helical arrangement gives rise to structural chirality in the system. Additionally, the in-plane projection of the dipole path forms a deformed polygon rather than a perfect circle (Fig. 1b), , a feature whose connection to the underlying C_4 symmetry of the strained crystal lattice will be discussed below.

These helical phases are associated with two distinct energy manifolds (green shading in Fig. 1c,d). The first, $\mathcal{M}_1$, is a lower-energy manifold corresponding to the calculated ground state. It is characterized by a dominant out-of-plane polarization and includes a

quasi-continuous set of states such as $\mathcal{S}1$, $\mathcal{S}2$, and $\mathcal{S}3$, with polarization tilt angles θ_z of 4°, 14°, and 32°, respectively. The second, $\mathcal{M}_2$, is a higher-energy, metastable manifold dominated by in-plane polarization, represented by states such as $\mathcal{S}4$ ($\theta_z = 87°$) and $\mathcal{S}5$ ($\theta_z \approx 90°$). As the system transitions from $\mathcal{S}1$ to $\mathcal{S}5$, the out-of-plane component $d_{\mathrm{Ti},z}$ decreases while the in-plane component $d_{\mathrm{Ti},xy}$ increases, corresponding to a larger tilt angle θ_z. The energy landscape associated with these helical phases resembles an asymmetric double-well potential. The two basins correspond to the $\mathcal{M}_1$ and $\mathcal{M}_2$ manifolds. Within each basin, the energy variation with respect to θ_z is relatively small, allowing for a quasi-continuous evolution of the tilt angle. The transition between the two manifolds is asymmetric: the energy barrier from $\mathcal{M}_1$ (e.g., $\mathcal{S}2$) to $\mathcal{M}_2$ (e.g., $\mathcal{S}4$) is approximately 8 meV/u.c., whereas the reverse barrier is less than 1 meV/u.c. This energy profile is consistent with a first-order structural phase transition and suggests that any field-driven switching between the two manifolds could involve notable hysteresis.

The physical origin of the two energy manifolds is examined using a phenomenological Landau-Ginzburg-Devonshire (LGD) model (see SM [14], Sec.II.C). The model suggests that the complex energy landscape can support multiple, nearly degenerate minima due to the high-dimensional parameter space involving coupled polarization components from both the Pb and Ti sublattices (in-plane and out-of-plane). For a fixed dipole spiral periodicity, different combinations of these sublattice polarizations can couple to produce states with comparable total energies, thereby giving rise to the $\mathcal{M}_1$ and $\mathcal{M}_2$ manifolds identified in the first-principles calculations.

A notable feature of the dipole spiral is its ability to support a rotational zero-energy mode. The emergence of this mode arises from the general property of embedding a helical distribution of vectors into any crystal lattice which exhibits the quadruple-well potential. For any idealized, polygonal helical arrangement (Fig. 2c, yellow stars), whether defined by the displacement of the Ti cation or by the net cell polarization, the global orientation can be specified by the in-plane polarization angle of the first layer, denoted φ_0. Once this angle is set, the orientations of all subsequent layers are determined by the helical relationship $\varphi_k = \varphi_0 + (k-1)\cdot 2\pi/N$, where k is the layer index. Although one might expect the system's total energy to depend on φ_0 due to the quadruple-well potential imposed by the strained lattice, our calculations show that for any periodicity $N \geq 3$ that is incommensurate with the underlying potential ($N \neq 4$), the total energy remains independent of φ_0 (Fig. 2a).

This results in an emergent $U(1)$ symmetry and an associated rotational zero-energy mode. The energy landscape as a function of the global angle φ_0 is analogous to a "Mexican-hat" potential, where the brim is flat (Fig. 2b). This introduces a qualitative difference in the degrees of freedom compared to conventional ferroelectric phases. In a rhombohedral-like (R) or monoclinic (M) phase, the energy is primarily determined by the orientation of a single polarization vector, typically specified by P_{xy} and P_z, within the potential landscape. In contrast, the dipole spiral is characterized by the collective distribution of polarization vectors across all layers. This arrangement introduces a continuous degree of freedom: the global in-plane phase angle φ_0. The flat energy profile along this coordinate gives rise to a rotational zero-energy mode, which manifests as the Goldstone mode [18, 19]. The existence of such a mode is expected to contribute to an enhanced response to external fields.

A subtlety arises in the precise nature of this Goldstone mode. At zero temperature, the system minimizes its energy by allowing the polarization vectors to relax slightly toward the four lowest-energy wells of the C_4 potential. This leads to a "deformed polygon" ground state rather than a perfectly symmetric configuration. Although the deformation is small, it weakly breaks the emergent $U(1)$ symmetry and introduces a finite energy gap in the rotational mode. The idealized "perfect polygon" state, which supports a true zero-energy mode, is therefore slightly higher in energy. Consequently, at 0 K, the weak pinning prevents the rotational mode from being truly energy-free. It is therefore more accurately characterized as a pseudo-Goldstone mode, or pseudo-zero-energy mode. This pinning, however, is fragile. The zero-energy character of the mode is gradually restored as the periodicity N increases, causing the deformed structure to approach the idealized configuration. Moreover, thermal fluctuations (k_BT) can readily overcome the small pinning energy (less than 1 meV/u.c.; see SM [14], Fig. S7), allowing the system to traverse the full rotational phase space, effectively recovering the behavior of a perfect polygon.

To better understand the microscopic nature of the dipole spiral, we performed a detailed analysis which reveals a structural complexity that extends beyond the simple helical ordering of net unit-cell dipoles. We found that all three constituent sublattices, Pb, Ti, and O, exhibit helical displacement patterns along the propagation axis (Fig. 2d). This hierarchical and intertwined helical ordering of the Pb-, Ti-, and O-sublattices can be conceptualized as an one-dimensional "self-moiré" crystal. In contrast to conventional moiré patterns, which are extrinsically generated at hetero-interfaces [20–23], this superlattice emerges intrinsically

within a single, homogeneous material under uniform strain.

In perovskite oxides, coupling between adjacent layers is often described in terms of the relative rotation of oxygen octahedra, typically categorized as either in-phase or out-of-phase, with the latter generally being energetically favorable [24]. However, a continuous, multi-layer helical rotation of the octahedra has not been widely considered, which may have contributed to the dipole spiral being previously overlooked. This collective chiral distortion of the lattice gives rise to two distinct local polarization vectors that form the basis of the dipole spiral: d_{Ti}, defined by the displacement of the Ti cation relative to the center of its surrounding oxygen octahedron (BO_6), and d_{Pb}, defined by the displacement within the Pb-centered AO_{12} cage. We find that these two local polarizations form distinct, intertwined helices that are intrinsically non-parallel (Fig. 2e). While both d_{Pb} and d_{Ti} follow helical paths, a stable, non-zero phase angle $\langle\phi\rangle = \frac{1}{N}\sum_{k=1}^{N}\phi_k$ exists between them. For the $\mathcal{M}_1$ ($\mathcal{M}_2$) state, this angle is calculated to be approximately 29° (35°). The non-parallelism reveals an internal, intra-cell degree of freedom and challenges the common approximation of representing unit-cell polarization as a single vector.

To quantify the energetics of this non-parallel configuration, we performed a model calculation in which an idealized "perfect polygon" double helix was constructed using the average d_{Pb} and d_{Ti} extracted from the fully relaxed (deformed) spiral ground state (also used in Fig. 2a). We then computed the total energy as a function of the relative phase angle ϕ, which is now equivalent to $\langle\phi\rangle$ (Fig. 2f). The resulting energy dependence exhibits a trigonometric form, consistent with predictions from the LGD model (see SM [14], Sec. II.D). In this double-helix configuration, while inter-helix interactions, quantified by the relative angle between the d_{Pb} and d_{Ti} helices, determine the absolute energy, they do not break the emergent $U(1)$ symmetry or gap the rotational zero-energy mode (Fig. 2f, φ_0 axis). The calculation reveals distinct energy minima (red stars) at phase angles of approximately 27° and 35°, in agreement with the values observed in the relaxed, deformed structures. This indicates that the non-parallel configuration is energetically favored. Furthermore, hypothetical configurations in which only a single cation sublattice forms a helix, or where both helices are aligned ($\phi = 0$), were found to be energetically unstable relative to the non-parallel ground state (see SM [14], Fig. S5). This finding was further corroborated by our finite-temperature molecular dynamics simulations (see SM [14], Fig. S6).

To explore the microscopic origin of this energy minimum, we turned to the LGD model

(see SM [14], Sec. II.E). We found that the stabilization of a non-zero phase angle could only be reproduced by introducing an emergent eDMI term between the two sublattice polarizations, of the form $\propto \mathcal{D}\cdot(d_{\mathrm{Pb}}\times d_{\mathrm{Ti}})$. This suggests that the collective chiral distortion of all three atomic sublattices breaks local inversion symmetry in a way that gives rise to an intrinsic eDMI. This interaction stabilizes the non-parallel double-helix configuration and offers a microscopic explanation for its energetic preference.

The unique topology of dipole spiral gives rise to an extraordinary piezoelectric response. To probe its electromechanical characteristics, we performed first-principles calculations of the out-of-plane polarization P_z as a function of out-of-plane strain η_z. The result, shown in Fig. 3a, reveals a giant and highly nonlinear piezoelectric response. Near the equilibrium state (η_z=0), we extract an intrinsic piezoelectric coefficient e_{33} of $\approx$16 C/m^2, a value roughly three-fold larger than that calculated for the T phase under identical strain conditions [25, 26] (see SM [14], Sec.IX).

This giant piezoelectricity originates from a unique, collective response mechanism rooted in dipole spiral's rotational pseudo-zero-energy mode. Unlike R-like or M phase, which respond to an out-of-plane perturbation through a rigid and energetically costly change in their polarization orientation, the dipole spiral evolves along a much lower-energy pathway. Instead, the pseudo-zero-energy mode provides a nearly resistance-free pathway for dipole spiral to evolve. The system can simultaneously execute an in-plane rotation, which consumes negligible energy, while making an infinitesimal adjustment to its tilt angle θ_z. The macroscopic piezoelectric response is thus the cumulative result of many such small, rotation-assisted tilting events, allowing the system to efficiently produce a large change in polarization for a minimal energy cost. This complex pathway is also responsible for the markedly anharmonic response, which directly reflects the non-parabolic shape of the flattened energy potential.

Under large cyclic strain, the system reveals its complex energy landscape through a hysteretic loop featuring first-order structural phase transitions between competing spiral manifolds $\mathcal{M}_1$ and $\mathcal{M}_2$. This hysteresis is a direct manifestation of their asymmetric energy barriers. Upon applying a critical compressive strain [(e)$\rightarrow$(f)], the high-P_z ($\mathcal{M}_1$) spiral undergoes an abrupt transformation into the low-P_z ($\mathcal{M}_2$) manifold. Once collapsed, the system is trapped until a critical tensile strain is applied [(g)$\rightarrow$(h)], causing it to jump back to the high-P_z ($\mathcal{M}_1$) state and completing the non-volatile switching cycle (see SM [14],

Sec.XI). Crucially, the critical tensile strain required for this "jump back" is not a fixed value but is dependent on the in-plane biaxial strain (see SM [14], Fig. S11). The link between helical topology and emergent functionality is proven by the system's behavior under extreme tensile strain. At η_z >3%, dipole spiral reversibly transforms into T-like phase (Fig. 3c). In this topologically trivial phase, the piezoelectric response immediately becomes linear and its magnitude reverts to that of a standard ferroelectric. This demonstrates that the giant piezoelectricity is an emergent property intrinsically bound to the helical topology.

It is important to consider the influence of finite temperature on this complex electromechanical response. At 0 K, the enhanced piezoelectricity originates from the pseudo-Goldstone mode associated with the rotational degree of freedom. At room temperature, the thermal energy ($k_{\mathrm{B}}T \approx 25$ meV) exceeds both the intra-manifold pinning potential (∼1 meV/u.c.) and the inter-manifold energy barrier (∼8 meV/u.c.). As a result, thermal fluctuations are expected to effectively restore a gapless Goldstone mode and render the $\mathcal{M}_1$ and $\mathcal{M}_2$ manifolds nearly degenerate. This thermally-induced degeneracy permits large-amplitude fluctuations of the polarization vector, potentially spanning the full tilt angle range $\theta_z = 0°$ to 90°. The collapse of the 0 K hysteresis under these conditions leads to an ultra-soft structural state, suggesting that the piezoelectric response at room temperature could be further enhanced.

Beyond its electromechanical properties, the chiral dipole spiral induces a reconstruction of the material's electronic structure, giving rise to an emergent multi-valley electronic topology. Our band structure calculations, performed using the band unfolding technique [27], reveal a manifold of degenerate local valence band maxima (VBMs) along the Γ–Z direction. These form a characteristic woven-shaped band structure (Fig. 4). The number of distinct VBMs, or valleys, denoted N_v, scales directly with the spiral periodicity N via $N_v = N/2$.

It is important to distinguish this multi-valley system from a flat band, despite the visually flat dispersion observed along the short Γ–Z k-path composed of multiple VBMs. Yet, it is precisely this emergence of quasi-flat bands that immediately brought moiré systems to mind, providing a key motivation for us to term the system a "self-moiré." A more definitive distinction is revealed through the density of states (DOS) analysis. In true flat-band systems, such as those observed in moiré heterostructures, a large number of electronic states are compressed into a narrow energy window, resulting in a sharp, high-intensity DOS peak, which plays a central role in driving strong electronic correlations [21,

28–30]. In contrast, our calculated DOS for the dipole spiral phase decreases smoothly and monotonically toward zero at the valence band edge. This indicates that each of the N_v valleys retains a normal, parabolic-like dispersion near its maximum. The total DOS is simply the superposition of these individual 3D-like valleys and therefore lacks the sharp peak associated with true electronic flatness. The key feature of this system is not a dispersionless state but rather the high degeneracy of multiple, structurally induced valleys.

This valley degeneracy could carry significant physical implications. Optically, it implies a highly degenerate excitonic ground state, which could give rise to complex fine-structure splitting and strong circular dichroism, reflecting the structure's intrinsic chirality. In terms of transport and many-body behavior, the presence of multiple valleys offers a pathway to a strongly correlated regime. Upon carrier (hole) doping, charge carriers are distributed among the N_v degenerate valleys. This reduces the carrier density per valley, thereby suppressing the intra-valley kinetic energy (i.e., the Fermi energy). Meanwhile, the long-range Coulomb interaction, governed by real-space carrier separation, remains unaffected. As a result, the ratio of potential to kinetic energy is significantly enhanced, potentially driving the system into an interaction-dominated, strongly correlated limit.

A possible consequence of such an interaction-dominated regime is the formation of a Wigner crystal [31], a collective state in which charge carriers freeze into a spatial lattice to minimize their mutual Coulomb repulsion. While the multi-valley topology originates in momentum space, its correlated consequences, such as real-space charge ordering, would manifest in the spatial domain and could be experimentally detectable under appropriate conditions. The dipole spiral thus offers a tunable platform for accessing and exploring strongly correlated electronic phenomena, enabled by its structural control over band degeneracy and carrier interactions.

In conclusion, we have discovered a chiral, non-collinear ferroelectric double helix in a strained ferroelectric oxide, characterized by intertwined, non-parallel helical polarizations of the Pb and Ti sublattices. This dipole spiral is stabilized by a collective helical lattice distortion that induces an emergent electronic Dzyaloshinskii-Moriya-like interaction, favoring a chiral ground state. The resulting "self-moiré" structure uniquely combines robust out-of-plane ferroelectricity with transverse helical order, giving rise to two coupled functionalities: a giant piezoelectric response ($e_{33} \approx 16$ C/m^2) driven by a rotational pseudo-zero-energy mode, and an emergent multi-valley electronic topology at the valence band edge. These

results demonstrate a strain-driven strategy for engineering polar topology, unifying structural chirality, strong electromechanical coupling, and correlated electronic behavior in a single phase. This work opens new directions for chiral phononic materials, high-sensitivity sensors, and tunable platforms for correlated electron physics.

Data availability — We have developed an online notebook [32] on Github to share the essential input and output files. Further details about DFT calculations using `VASP` [33, 34] can be found in Supplementary Material [14].

ACKNOWLEDGMENTS

We acknowledge the supports from Zhejiang Provincial Natural Science Foundation of China (LR25A040004). The computational resource is provided by Westlake HPC Center.

[1] B. Rodriguez, X. Gao, L. Liu, W. Lee, I. Naumov, A. Bratkovsky, D. Hesse, and M. Alexe, Vortex polarization states in nanoscale ferroelectric arrays, Nano Lett. **9**, 1127 (2009).

[2] N. Balke, B. Winchester, W. Ren, Y. H. Chu, A. N. Morozovska, E. A. Eliseev, M. Huijben, R. K. Vasudevan, P. Maksymovych, J. Britson, S. Jesse, I. Kornev, R. Ramesh, L. Bellaiche, L. Q. Chen, and S. V. Kalinin, Enhanced electric conductivity at ferroelectric vortex cores in $BiFeO_3$, Nat. Phys. **8**, 81 (2012).

[3] A. K. Yadav, Observation of polar vortices in oxide superlattices, Nature **530**, 198 (2016).

[4] S. Das, Observation of room-temperature polar skyrmions, Nature **568**, 368 (2019).

[5] L. Han, C. Addiego, S. Prokhorenko, M. Wang, H. Fu, Y. Nahas, X. Yan, S. Cai, T. Wei, Y. Fang, *et al.*, High-density switchable skyrmion-like polar nanodomains integrated on silicon, Nature **603**, 63 (2022).

[6] Y. Wang, Y. Feng, Y. Zhu, Y. Tang, L. Yang, M. Zou, W. Geng, M. Han, X. Guo, B. Wu, *et al.*, Polar meron lattice in strained oxide ferroelectrics, Nat. Mater. **19**, 881 (2020).

[7] R. Ramesh and D. G. Schlom, Creating emergent phenomena in oxide superlattices, Nat. Rev. Mater. **4**, 257 (2019).

[8] I. Gross, W. Akhtar, V. Garcia, L. J. Martínez, S. Chouaieb, K. Garcia, C. Carrétéro, A. Barthélémy, P. Appel, P. Maletinsky, J.-V. Kim, J. Y. Chauleau, N. Jaouen, M. Viret,

M. Bibes, S. Fusil, and V. Jacques, Real-space imaging of non-collinear antiferromagnetic order with a single-spin magnetometer, Nature **549**, 252 (2017).

[9] D. Sando, A. Agbelele, D. Rahmedov, J. Liu, P. Rovillain, C. Toulouse, I. C. Infante, A. P. Pyatakov, S. Fusil, E. Jacquet, C. Carrétéro, C. Deranlot, S. Lisenkov, D. Wang, J.-M. Le Breton, M. Cazayous, A. Sacuto, J. Juraszek, A. K. Zvezdin, L. Bellaiche, B. Dkhil, A. Barthélémy, and M. Bibes, Crafting the magnonic and spintronic response of $BiFeO_3$ films by epitaxial strain, Nat. Mater. **12**, 641 (2013).

[10] D. D. Khalyavin, R. D. Johnson, F. Orlandi, P. G. Radaelli, P. Manuel, and A. A. Belik, Emergent helical texture of electric dipoles, Science **369**, 680 (2020).

[11] Y. Hu, J. Yang, and S. Liu, Giant piezoelectric effects of topological structures in stretched ferroelectric membranes, Phys. Rev. Lett. **133**, 046802 (2024).

[12] I. Dzyaloshinsky, A thermodynamic theory of "weak" ferromagnetism of antiferromagnetics, J. Phys. Chem. Solids **4**, 241 (1958).

[13] H. J. Zhao, P. Chen, S. Prosandeev, S. Artyukhin, and L. Bellaiche, Dzyaloshinskii-moriya-like interaction in ferroelectrics and antiferroelectrics, Nat. Mater. **20**, 341 (2021).

[14] See supplemental material at [url], which includes Refs. [11, 27, 33–42], for additional discussions on Landau-Ginzburg-Devonshire model, and more details for dipole spirals.

[15] Y. Tsunoda, Spin-density wave in cubic γ-Fe and γ-$Fe_{100-x}Co_x$ precipitates in Cu, J. Phys. Condens. Matter **1**, 10427 (1989).

[16] Y. Tsunoda, Y. Nishioka, and R. Nicklow, Spin fluctuations in small γ-Fe precipitates, J. Magn. Magn. Mater. **128**, 133 (1993).

[17] R. D. King-Smith and D. Vanderbilt, Theory of polarization of crystalline solids, Phys. Rev. B **47**, 1651 (1993).

[18] J. Goldstone, A. Salam, and S. Weinberg, Broken symmetries, Phys. Rev. **127**, 965 (1962).

[19] A. Marthinsen, S. M. Griffin, M. Moreau, T. Grande, T. Tybell, and S. M. Selbach, Goldstone-like phonon modes in a (111)-strained perovskite, Phys. Rev. Mater. **2**, 014404 (2018).

[20] R. Bistritzer and A. H. MacDonald, Moiré bands in twisted double-layer graphene, Proc. Natl. Acad. Sci. **108**, 12233 (2011).

[21] Y. Cao, V. Fatemi, S. Fang, K. Watanabe, T. Taniguchi, E. Kaxiras, and P. Jarillo-Herrero, Unconventional superconductivity in magic-angle graphene superlattices, Nature **556**, 43 (2018).

[22] A. Timmel and E. J. Mele, Dirac-harper theory for one-dimensional moiré superlattices, Phys. Rev. Lett. **125**, 166803 (2020).

[23] Y. Bai, L. Zhou, J. Wang, W. Wu, L. J. McGilly, D. Halbertal, C. F. B. Lo, F. Liu, J. Ardelean, P. Rivera, N. R. Finney, X.-C. Yang, D. N. Basov, W. Yao, X. Xu, J. Hone, A. N. Pasupathy, and X.-Y. Zhu, Excitons in strain-induced one-dimensional moiré potentials at transition metal dichalcogenide heterojunctions, Nat. Mater. **19**, 1068 (2020).

[24] J. R. Kim, J. Jang, K.-J. Go, S. Y. Park, C. J. Roh, J. Bonini, J. Kim, H. G. Lee, K. M. Rabe, J. S. Lee, S.-Y. Choi, T. W. Noh, and D. Lee, Stabilizing hidden room-temperature ferroelectricity via a metastable atomic distortion pattern, Nat. Commun. **11**, 4944 (2020).

[25] Z. Li, M. Grimsditch, C. Foster, and S.-K. Chan, Dielectric and elastic properties of ferroelectric materials at elevated temperature, J. Phys. Chem. Solids **57**, 1433 (1996).

[26] G. Sághi-Szabó, R. E. Cohen, and H. Krakauer, First-principles study of piezoelectricity in pbtio$_3$, Phys. Rev. Lett. **80**, 4321 (1998).

[27] V. Popescu and A. Zunger, Extracting E versus $\vec{k}$ effective band structure from supercell calculations on alloys and impurities, Phys. Rev. B **85**, 085201 (2012).

[28] M. L. Kiesel, C. Platt, and R. Thomale, Unconventional fermi surface instabilities in the kagome hubbard model, Phys. Rev. Lett. **110**, 126405 (2013).

[29] L. Van Hove, The occurrence of singularities in the elastic frequency distribution of a crystal, Phys. Rev. **89**, 1189 (1953).

[30] M. Kang, S. Fang, J.-K. Kim, B. R. Ortiz, S. H. Ryu, J. Kim, J. Yoo, G. Sangiovanni, D. Di Sante, B.-G. Park, C. Jozwiak, A. Bostwick, E. Rotenberg, E. Kaxiras, S. D. Wilson, J.-H. Park, and R. Comin, Twofold van hove singularity and origin of charge order in topological kagome superconductor CsV_3Sb_5, Nat. Phys. **18**, 301 (2022).

[31] E. Wigner, On the interaction of electrons in metals, Phys. Rev. **46**, 1002 (1934).

[32] https://github.com/huiihao/Spiral_DFT, Available online.

[33] G. Kresse and J. Furthmüller, Efficient iterative schemes for ab initio total-energy calculations using a plane-wave basis set, Phys. Rev. B **54**, 11169 (1996).

[34] G. Kresse and J. Furthmüller, Efficiency of ab-initio total energy calculations for metals and semiconductors using a plane-wave basis set, Comput. Mater. Sci. **6**, 15 (1996).

[35] P. E. Blochl, Projector augmented-wave method, Phys. Rev. B **50**, 17953 (1994).

[36] G. Kresse and D. Joubert, From ultrasoft pseudopotentials to the projector augmented-wave

method, Phys. Rev. B **59**, 1758 (1999).

[37] J. P. Perdew, A. Ruzsinszky, G. I. Csonka, O. A. Vydrov, G. E. Scuseria, L. A. Constantin, X. Zhou, and K. Burke, Restoring the density-gradient expansion for exchange in solids and surfaces, Phys. Rev. Lett. **100**, 136406 (2008).

[38] R. Xu, J. Huang, E. S. Barnard, S. S. Hong, P. Singh, E. K. Wong, T. Jansen, V. Harbola, J. Xiao, B. Y. Wang, S. Crossley, D. Lu, S. Liu, and H. Y. Hwang, Strain-induced room-temperature ferroelectricity in $SrTiO_3$ membranes, Nat. Commun. **11**, 3141 (2020).

[39] S. S. Hong, M. Gu, M. Verma, V. Harbola, B. Y. Wang, D. Lu, A. Vailionis, Y. Hikita, R. Pentcheva, J. M. Rondinelli, and H. Y. Hwang, Extreme tensile strain states in $La_{0.7}Ca_{0.3}MnO_3$ membranes, Science **368**, 71 (2020).

[40] L. Han, X. Yang, Y. Lun, Y. Guan, F. Huang, S. Wang, J. Yang, C. Gu, Z.-B. Gu, L. Liu, Y. Wang, P. Wang, J. Hong, X. Pan, and Y. Nie, Tuning piezoelectricity via thermal annealing at a freestanding ferroelectric membrane, Nano Lett. **23**, 2808 (2023).

[41] J. Shaju, E. Pavlovska, R. Suba, J. Wang, S. Ouacel, T. Vasselon, M. Aluffi, L. Mazzella, C. Geffroy, A. Ludwig, A. D. Wieck, M. Urdampilleta, C. Bäuerle, V. Kashcheyevs, and H. Sellier, Evidence of coulomb liquid phase in few-electron droplets, Nature **642**, 928 (2025).

[42] N. D. Mermin, The topological theory of defects in ordered media, Rev. Mod. Phys. **51**, 591 (1979).

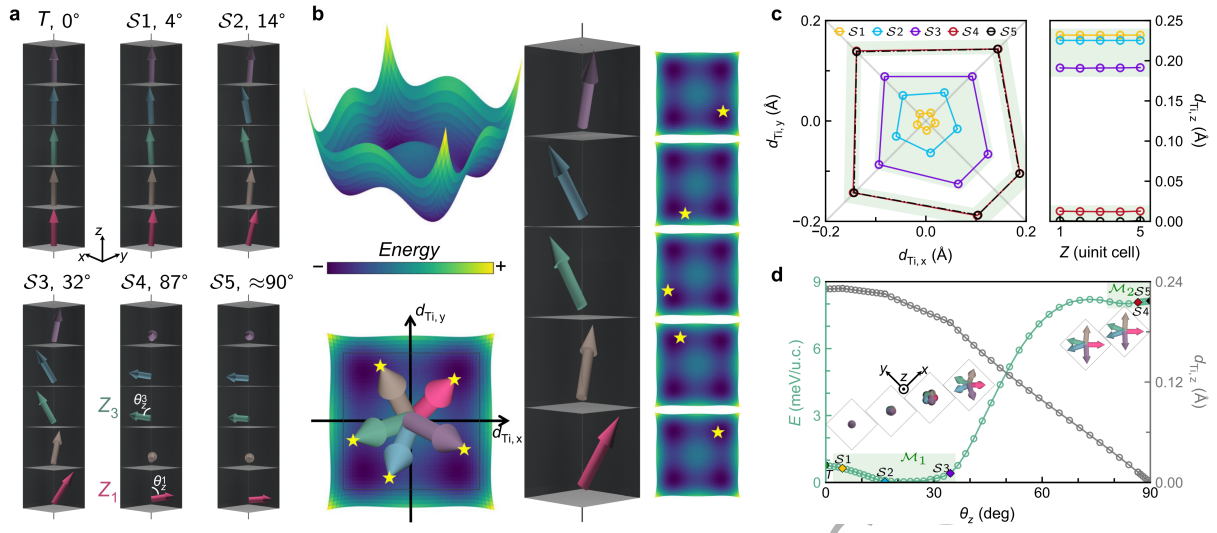

FIG. 1. **A Family of Dipole helical phases and Their Energetic Landscape.** (a) Schematics of T and stable dipole helical phases ($\mathcal{S}1$-$\mathcal{S}5$) in strained ($a = b = 3.970$ Å) $PbTiO_3$, distinguished by their polarization tilt angle $\theta_z = \frac{1}{N}\sum_{k=1}^{N}\theta_z^k$. (b) The quadruple-well potential energy surface arising from the C_4 symmetry of the strained lattice. The yellow stars represent the in-plane polarization vectors ($d_{\mathrm{Ti},xy}$) for each of the five layers of a representative helical phase, illustrating how the polarization is energetically favored to lie within the potential wells. (c) The left panel shows the top-down view of dipole spiral's in-plane polarization path, formed by connecting the vertices (the yellow stars) from (b). This path is a deformed polygon, a direct consequence of the pinning effect of the quadruple-well potential. The right panel plots the out-of-plane polarization component ($d_{\mathrm{Ti},z}$) as a function of the layer index (Z). (d) Energy and $d_{\mathrm{Ti},z}$ landscape along a linear interpolation path between T-$\mathcal{S}1$-$\mathcal{S}5$. The insets are the top view of the schematics in (a), corresponding to the left panel of (b).

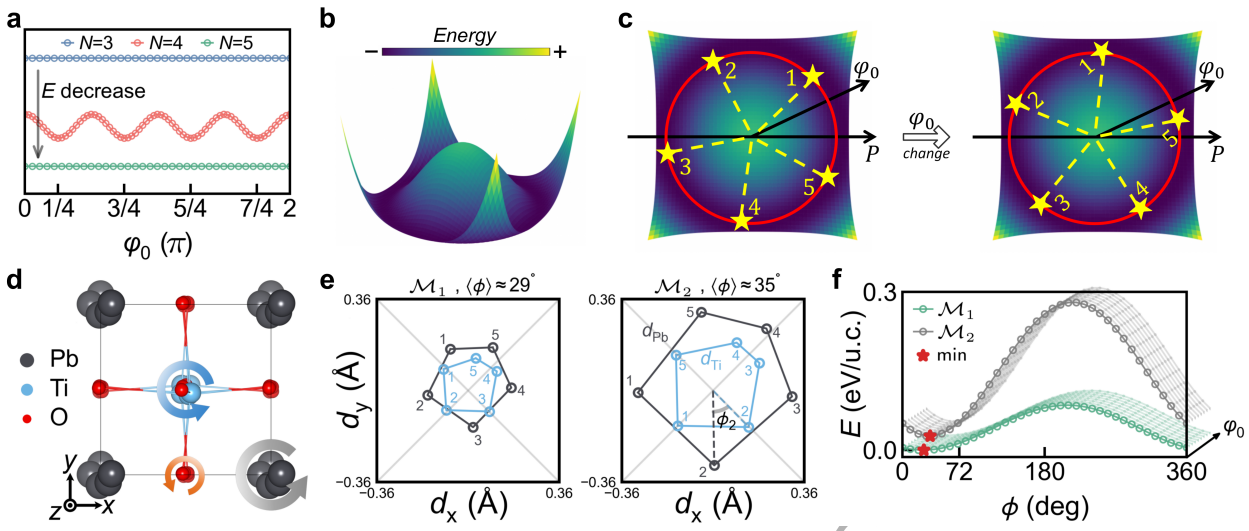

FIG. 2. **Microscopic Origin and Dynamics of the Ferroelectric Double Helix.** (a) Total energy as a function of the global in-plane orientation φ_0. When the ϕ is fixed, the energy is independent of φ_0; Therefore, the addition of the φ_0 axis in (f) causes the curves to exhibit repetitive and consistent three-dimensional shadows. (b) A conceptual, three-dimensional representation of the "Mexican-hat" potential energy surface that describes the collective rotational dynamics of an idealized spiral. (c) Illustration of the Goldstone mode for an idealized N=5 "perfect pentagon" spiral. The left panel shows a schematic of this state, where the in-plane polarization vectors of the five layers (yellow stars) are equally spaced on a circle (red), with a fixed 72° angle between adjacent layers. The collective rotation of this idealized spiral is a zero-energy process (right panel). (d) Top view of the relaxed supercell, revealing the intertwined helical nature of the Pb- (gray) and Ti-sublattice (blue) polarizations, which form a double helix with a non-parallel phase angle $\langle\phi\rangle$ for both (e, left panel) $\mathcal{M}_1$ and (e, right panel) $\mathcal{M}_2$ (right) spirals. (f) Total energy as a function of the relative phase angle ϕ between $d_{\mathrm{Ti},xy}$ and $d_{\mathrm{Pb},xy}$.

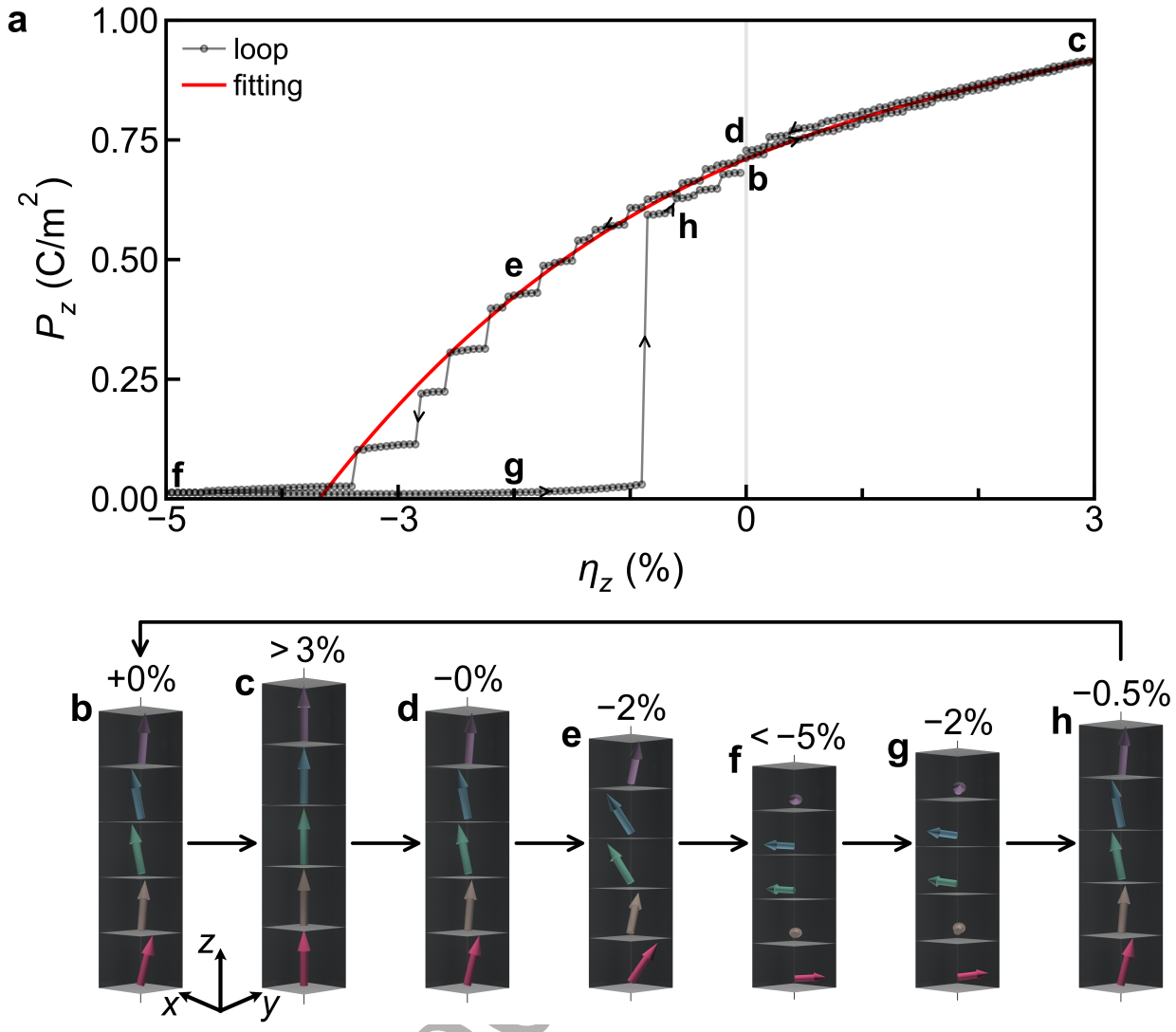

FIG. 3. **Giant and Hysteretic Electromechanical Response.** (a) Calculated out-of-plane polarization (P_z) versus uniaxial strain (η_z) for the $\mathcal{S}2$ spiral. The reversible response near equilibrium (red curve) is highly anharmonic, yielding a giant piezoelectric coefficient $e_{33} \approx 16$ C/m^2. The large loop demonstrates hysteretic, first-order switching between two manifolds. (b-h) Snapshots of the dipole configurations at key points in the strain cycle, illustrating the initial $\mathcal{S}2$ state (b), the irreversible collapse to a low-P_z state ($\mathcal{M}_2$) under compression [(e)→(f)], and the transformation to a topologically trivial T phase under large tension [(b)→(c)].

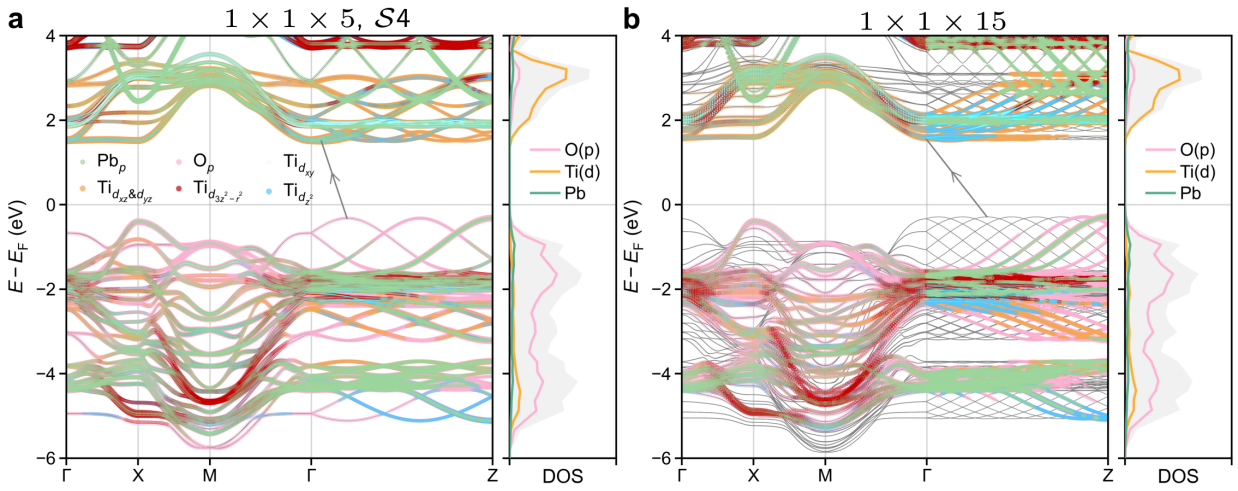

FIG. 4. **Electronic Structure Reconstruction and Multi-Valley Topology.** Unfolded band structures and corresponding projected density of states (PDOS) for dipole spirals when (a) N=5 and (b) N=15. A manifold of nearly-degenerate local valence band maxima (VBMs) emerges along the Γ-Z direction (spiral propagation axis).